animals

MDPI

Article

Can a Red Wood-Ant Nest Be Associated with Fault-Related CH_4 Micro-Seepage? A Case Study from Continuous Short-Term In-Situ Sampling

Gabriele M. Berberich [1,*], Aaron M. Ellison [2], Martin B. Berberich [3], Arne Grumpe [1], Adrian Becker [1] and Christian Wöhler [1]

1 Image Analysis Group, Faculty of Electrical Engineering and Information Technology, Technical University of Dortmund, 44221 Dortmund, Germany; Arne.Grumpe@tu-dortmund.de (A.G.); Adrian.Becker@tu-dortmund.de (A.B.); christian.woehler@tu-dortmund.de (C.W.)
2 Harvard Forest, Harvard University, 324 North Main Street, Petersham, MA 01366, USA; aellison@fas.harvard.edu
3 IT-Consulting Berberich, 50374 Erftstadt, Germany; mb@berberichweb.com
* Correspondance: gabriele.berberich@tu-dortmund.de

Received: 20 February 2018; Accepted: 25 March 2018; Published: 28 March 2018

Simple Summary: Methane (CH_4) is common on Earth but its natural sources are not well-characterized. We investigated concentrations of CH_4 and its stable carbon isotope (δ^{13}C-CH_4) within a red wood-ant (RWA; *Formica polyctena*) nest in the Neuwied Basin, a part of the East Eifel Volcanic Field (EEVF), and tested for associations between methane concentration and RWA activity patterns, earthquakes, and earth tides. Methane degassing was not synchronized with earth tides, nor was it influenced by a micro-earthquake or RWA activity. Elevated CH_4 concentrations in nest gas appear to result from a combination of microbial activity and fault-related emissions. The latter could result from micro-seepage of methane derived from low-temperature gas-water-rock reactions that subsequently moves via fault networks through the RWA nest or from overlapping micro-seepage of magmatic CH_4 from the Eifel plume. Given the abundance of RWA nests on the landscape, their role as sources of microbial CH_4 and biological indicators for abiotically-derived CH_4 should be included in estimations of methane emissions that are contributing to climatic change.

Abstract: We measured methane (CH_4) and stable carbon isotope of methane (δ^{13}C-CH_4) concentrations in ambient air and within a red wood-ant (RWA; *Formica polyctena*) nest in the Neuwied Basin (Germany) using high-resolution in-situ sampling to detect microbial, thermogenic, and abiotic fault-related micro-seepage of CH_4. Methane degassing from RWA nests was not synchronized with earth tides, nor was it influenced by micro-earthquake degassing or concomitantly measured RWA activity. Two δ^{13}C-CH_4 signatures were identified in nest gas: −69‰ and −37‰. The lower peak was attributed to microbial decomposition of organic matter within the RWA nest, in line with previous observations that RWA nests are hot-spots of microbial CH_4. The higher peak has not been reported in previous studies. We attribute this peak to fault-related CH_4 emissions moving via fault networks into the RWA nest, which could originate either from thermogenic or abiotic CH_4 formation. Sources of these micro-seepages could be Devonian schists, iron-bearing "Klerf Schichten", or overlapping micro-seepage of magmatic CH_4 from the Eifel plume. Given the abundance of RWA nests on the landscape, their role as sources of microbial CH_4 and biological indicators for abiotically-derived CH_4 should be included in estimation of methane emissions that are contributing to climatic change.

Keywords: red wood ants; *Formica polyctena*; CH_4; δ ^{13}C-CH_4; fault; activity pattern

1. Introduction

Methane (CH_4) is common on Earth, forms the major commercial natural gas reservoirs, and is a key component of the global carbon cycle [1,2]. This second-most important greenhouse gas currently has an average atmospheric concentration of 1.82 ppm, and continues to increase [3]. Today, most natural occurrences of CH_4 are associated with terrestrial and aquatic processes. In the shallow subsurface, CH_4 is produced on geological time scales mainly by thermal conversion of organic matter resulting from heat and pressure deep in the Earth's crust or by microbial activity. This biotic CH_4, which forms the major commercial natural gas reservoirs, derives from thermogenic CH_4, chemical reactions of inorganically derived gases such as carbon dioxide (CO_2), carbon monoxide (CO), and hydrogen (H_2), and microbial aceticlastic methanogenesis [2,4,5]. In contrast, abiotic CH_4 is produced in much smaller amounts and does not form economically exploitable reserves [2]. It is formed by chemical reactions that do not directly include organic matter, either during high-temperature magmatic processes (Sabatier-type reactions) in volcanic and geothermal areas, or via low-temperature (<100 °C) Fischer-Tropsch-Type (FTT) reactions between gas, water and rock in continental settings, which also may occur at shallow depths [2]. This abiotic CH_4 is found in specific geologic environments, including volcanic and geothermal systems; fluid inclusions in igneous intrusions; crystalline rocks in Precambrian Shields; and submarine, serpentinite-hosted hydrothermal fields or land-based serpentinization fluids [2,4].

In most geologic environments, however, biotic and abiotic gases co-occur. Both thermogenic and abiotic CH_4 reach the atmosphere through marine and terrestrial geologic gas (micro-)seeps, and during the exploitation and distribution of fossil fuels. To identify whether locally elevated CH_4 concentrations in the atmosphere result from transportation via fault networks, a determination of possible methane source(s) is required. At the land surface, CH_4 is produced by methanogenic Archaea in anaerobic soil environments or through oxidation by methanotrophic bacteria in aerobic topsoils [6]. Isotopic measurements of δ^{13}C-CH_4, ideally in combination with ^{13}H [1,7,8], can distinguish abiotic from biotic CH_4 [7,8].

Increase of the compressive stress, volume changes of the pore fluid or rock matrix, and movement or buoyancy of the fluid are important mechanisms driving fluid flow and keeping fractures open [9,10]. The preferential pathways of lateral and vertical degassing are faults and fracture networks, creating linear anomalies connected to faults, diffuse or "halo" anomalies of irregular shape, and irregularly-spaced plumes or "spot anomalies" (e.g., [11,12]). Boothroyd et al. [10] showed that faults had δ^{13}C-CH_4 = −37‰ and a significantly higher CH_4 flux (11.5 ± 6.3 t CH_4 km^{-1} yr^{-1}) than control zones. In Europe, micro-seeps occur both onshore and offshore, with estimated CH_4 flux in Europe of 0.8 Tg yr^{-1} and total seepage of 3 Tg yr^{-1} [5,12].

Recent research has revealed close spatial relationships between red wood-ant nests (*Formica rufa*-group; henceforth RWA) and tectonic fault zones [13–16]. Exploratory testing of fault-zone gases revealed that helium (He) and radon (Rn) in RWA nests exceeded atmospheric and background concentrations [13,14]. RWA mounds also have been found to be "hot spots" for CO_2 emissions in European forests that increase the heterogeneity of soil carbon (C) emissions in forest ecosystems [17–20]. Wu et al. [21] showed that ant mounds (*Lasius flavus*, *Lasius niger* and *Formica candida*) contributed measurable amounts of CO_2 and N_2O to soil gas emissions from wetlands (CO_2: 7.02% and N_2O: 3.35%), but act as sinks with respect to the total soil CH_4 budget (−4.28%); this relationship strongly depends on soil type. In contrast, higher net CH_4 emission (3.5 µg m^{-2} h^{-1}) were found in fire ant (*Solenopsis invicta*) mounds in natural pasture soils [22]. However, continuous in-situ sampling of natural release of CH_4 from RWA nests has not been done. Jílková et al. [6] estimated CH_4 flux from sampled nest material that was collected from the top and the rim of each of five nests on two different days (30 July and 14 October) in 2014. Finally, natural release of CH_4 via fault zones [10] has been rarely considered, although there are a range of processes that could contribute to it, including micro-seepage via buoyant flux of CH_4, faults increasing the flow rate of microbubbles, and gas vents responding to earth tides and earthquakes [23,24].

We used a combination of geochemical, geophysical, and biological techniques, state-of-the-art image analysis,and statistical methods to identify associations between RWA activity, continuous in-situ CH_4 degassing, earth tides, and tectonic processes. We aimed to test, from a geochemical/geophysical point of view, three different hypothesis: (a) whether a RWA nest is associated with actively in-situ degassing faults trapping migrating CH_4 from the deep underground; (b) whether RWA activity changes during the CH_4 (micro)-seepage process; and (c) whether CH_4 (micro)-seepage processes are affected by external agents (earth tides, earthquake events, or meteorological conditions). Specifically, we tested the null hypotheses that, in the field, in-situ concentrations of both CH_4 and δ^{13}C-CH_4 and RWA activity are independent. We found that a RWA nest appears to be associated with fault-related micro-seepage of CH_4, and that degassing patterns are independent from earth tides and meteorological conditions.

2. Methods

We explored associations between RWA activity, in-situ methane concentrations in an ant nest and ambient air, tectonic events, weather, and earth tides at the Goloring site near Koblenz, Germany during a continuous, in-situ 8-day sampling campaign (4–11 August 2016). Time and duration of the CH_4 sampling was determined by the availability of the CRDS analyser owned by the Institute for Geosciences (University of Heidelberg, Heidelberg, Germany). Our in-situ approach contrasts with prior work where different nests were statically sampled and CH_4 flux was estimated in the laboratory from 10 nest-material samples (e.g., [6]).

2.1. Study Area

The Goloring site is located west of the Rhine River, southeast of the Laacher See volcano, and close to the Ochtendung Fault Zone in the seismically active Neuwied Basin, which is part of the Quaternary East Eifel Volcanic field (EEVF; western Germany; Figure 1a). The EEVF includes ≈100 Quaternary volcanic eruption centres; the Laacher See volcano experienced a phreato-plinian eruption ≈12,900 years ago [25]. The Paleozoic basement consists of alternating strata of Devonian, iron-bearing, quartzitic sandstones with a carbonate matrix and argillaceous shale reaching to 5-km depths. Several thin black coal seams (Upper Siegen) are embedded within these alternating strata [26]. Ecocene/Oligocene lignite seams are found at ≈75–160 m and are covered by Paleogene volcanites and Neogene clastic sediments. The study area has been affected by complex major tectonic and magmatic processes, including plume-related thermal expansion of the mantle-lithosphere [27–29], crustal thinning and associated volcanism [30], active rifting processes [31], and possibly crustal-scale folding or the reactivation of Variscan thrust faults under the present-day NW–SE-directed compressional stress field [31,32]. Those processes can be attributed to old zones of weakness reactivated by the current stress field [29,33,34]. Earthquakes (Figure 1a) are concentrated in areas that are related to the seismically active Ochtendunger Fault Zone [33]. These earthquakes are related to stress-field-controlled block movements, have a weak-to-moderate seismicity, and occur mostly in a shallow crustal depth ($\leq$15 km) with local magnitudes (Richter scale) rarely exceeding 4.0. No fault zones have been reported from our Goloring study site and focal depth of earthquakes near the site never exceeded 28 km during our sampling campaign [35].

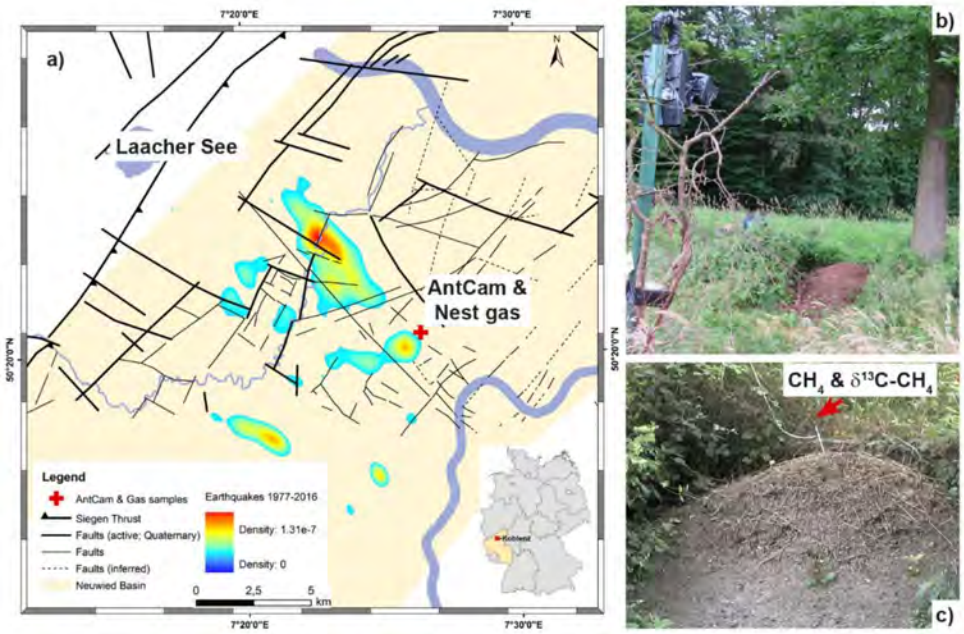

Figure 1. Location of the Goloring study area within the Neuwied Basin. The map (**a**) shows the Goloring study site (red cross) ≈15 km SE of the Laacher See volcano within the Neuwied Basin (light yellow area), tectonic structures (black lines) and probability density of the earthquake events from 1977–2016 which are related to the Ochtendunger Fault Zone (rainbow contours). The inset shows the location of study site within Germany. Photographs show (**b**) the AntCam for continuous monitoring of ant activity and (**c**) the nest gas probe (all photographs: Gabriele M. Berberich).

2.2. Monitoring Red Wood Ant Activity

At the Goloring site, the density of red wood ant nests is ≈9 nests/ha. Within the research project "GeoBio-Interactions" (March–September 2016), we monitored RWA activity using an "AntCam": a high-resolution camera system (Mobotix MX-M12D-Sec-DNight-D135N135, Langmeil, Germany; 1280 × 960 pixels) installed ≈5 m from a partly sunlit RWA nest (height: 0.70 m; diameter: 2.20 m) located close to an oak tree (Figure 1b). During the 192-h CH_4 sampling campaign, which ran from 4–11 August 2016, ant activities were recorded at 12 Hz and time-stamped continuously. The network-compatible AntCam was connected to a network-attached storage (NAS) system for data storage via a power-over-Ethernet (POE) supply. A computer connected to the NAS evaluated RWA activities on-site and in real time using the self-developed C++ code to accelerate image evaluation. Image analysis extended the system of [36] and was based on the difference image technique (Figure 2). To reduce negative influences caused by, for example, moving blades of grass, we used a mask to restrict analysis to only the visible top of the mound. To compensate for slight movements of the camera, for example, due to wind, an image registration of the current image relative to the previous image was done based on mutual information before the determination of the absolute difference image [37]. Results of RWA activity were written to a file. Every hour, this file was sent via email (mobile data transfer, long-term evolution (LTE) router) to a mail server. Since two different sensors were used for the day and night, respectively, we computed different polynomials to map the sum of absolute differences onto manually designed activity categories in a follow-up procedure. The coefficients of the polynomials were obtained from a minimization of the sum of squared differences between the polynomial model and the manually assigned category for two selected weeks. A first-order polynomial was adapted to the daytime data and a third-order polynomial was adapted to the nighttime data. To avoid numerical difficulties, we first centered and scaled the data by subtracting the mean of the data during the target time and dividing by the standard deviation. Both values were computed for day- and nighttime, respectively.

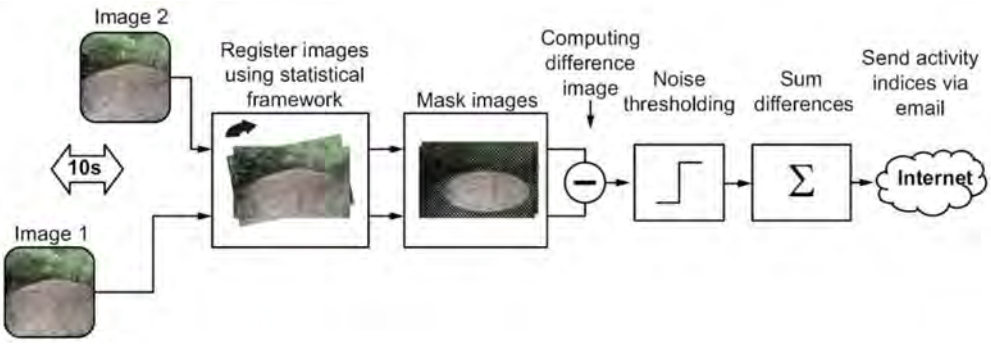

Figure 2. Workflow for acquisition and estimation of red wood-ant (RWA) activity. The "AntCam", a network-compatible high-resolution camera system, was connected to a network-attached storage (NAS) system for data storage via a power-over-Ethernet (POE) supply. A computer connected to the NAS evaluated the RWA activities on-site and in real time using the self-developed C++ code to accelerate image evaluation. Image analysis extended the system of [36] and was based on the difference image technique. Results of RWA activity were written to a file. Every hour, this file was sent via email (mobile data transfer, long-term evolution (LTE) router) to a mail server.

2.3. Gas Sampling and Geochemical Analyses

Field measurements of CH_4 were taken from 4–11 August 2016. A stainless-steel probe (inner diameter 0.6 cm; Figure 1c) was used for continuous $CH_4/\delta^{13}C\text{-}CH_4$ measurements. It was equipped with a flexible tip attached to a pushable rod and a sealable outlet for docking sampling equipment. The closed probe was inserted into the *F. polyctena* nest without requiring force to a depth of 80 cm to prevent atmospheric influences [38] and remained there, unmoved, during the entire 192-h sampling campaign. After opening by pushing the rod, the probe was evacuated twice, using a 20-mL syringe. After this, the outlet was closed to prevent atmospheric influence. The outlet was only opened after docking the sampling unit to it.

Concentrations of CH_4 and $\delta^{13}C\text{-}CH_4$ in nest gas (NG) and ambient air (AA) were monitored using a portable CRDS analyser (G2201-i; Picarro, Santa Clara, CA, USA) that measured $^{12}CH_4$, $^{13}CH_4$ and H_2O quasi-simultaneously at 1 Hz, and provided ^{13}C values relative to the Vienna Pee Dee Belemnite standard. The G2201-i uses built-in pressure and temperature control systems, and automatic water-vapor correction to ensure high stability of the portable analyzer. Effects of water vapor on the measurement were corrected automatically by the Picarro® software (Santa Clara, CA, USA). The manufacturer guarantees concentration precision for the analysis of CH_4 in the "high precision mode" of 5 ppbv $\pm$ 0.05 % (^{12}C) and 1 ppbv $\pm$ 0.05% (^{13}C) within a concentration range of 1.8–1000 ppm. The guaranteed precision of $\delta^{13}C\text{-}CH_4$ is <0.8‰.

The CRDS analyzer was deployed in a dry, wind-sheltered location near the RWA nest. Nest gases were pumped from the aforementioned probe into the CRDS analyzer for analysis of CH_4 and $\delta^{13}C\text{-}CH_4$ values. Ambient air was measured 2 m away from the nest for 15 min every four hours during the operation using a 3-way-valve, avoiding disturbance of the nest or the position of the steel probe. All gases passed through a chemical trap filled Ascarite® (sodium hydroxide coated silica; www.merckgroup.com) before entering the system to remove carbon dioxide (CO_2), as the high concentrations of CO_2 in the nest samples could interfere with the measurements of CH_4 and $\delta^{13}C\text{-}CH_4$. Gas samples were dried by a Nafion® drying tube (Nafion MD110, PermaPure LLC, Lakewood, NJ, USA) before measurements to ensure higher accuracy and subsequently analyzed for CH_4 concentration and $\delta^{13}C\text{-}CH_4$. To assure quality of the CH_4 and $\delta^{13}C\text{-}CH_4$ values, reference gas measurements were taken every 8 h during the operation. Fluctuations in atmospheric CH_4 and $\delta^{13}C\text{-}CH_4$ values were validated against a single, 4-h measurement of ambient air. Carbon isotope ratios are expressed using standard delta (δ) notation according to the deviation from a standard: $\delta_{sample}‰ = ((R_{sample}/R_{standard} - 1)) \times 1000$, where R is the $^{13}C/^{12}C$ ratio in the sample or standard.

A total of 459 704 samples for both CH_4 and δ^{13}C-CH_4 in nest gas and 27 samples in ambient air were collected and analyzed.

2.4. Meteorological Parameters

A radio meteorological station (WH1080) placed 2 m above the ground at the Goloring site continuously logged meteorological conditions (temperature (°C), humidity (%), air pressure (hPa), wind speed (m/s), rainfall (mm), and dew point (°C)) at 5-min intervals. The recorded data were downloaded every two days, checked for completeness, and stored in a data base.

2.5. Earth Tides

Cyclic changes in the Earth's environment are caused by the gravitational pull of both the Sun and the Moon on the earth. These result in two slight lunar and solar tidal bulges ("earth tides"). The two bulges occur at the surface of the earth that approximately faces the Moon and at the opposite side while the Earth rotates around its axis. Earth tides were calculated using the tool developed by Milbert [39].

2.6. Earthquake Events

Data on earthquake events during the sampling campaign were obtained from the seismological databases provided by the Erdbebenstation Bensberg ([35], www.seismo.uni-koeln.de/events/index.htm) and by the Landesamt für Geologie und Bergbau, Rheinland-Pfalz ([40], http://www.lgb-rlp.de/fachthemen-des-amtes/landeserdbebendienst-rheinland-pfalz/). The probability density of the earthquake events was estimated using the kernel density estimator of [41] using Gaussian kernels.

2.7. Data Analysis

All analyses were done using R version 3.3.2 (R Core Team 2016, www.R-project.org) or MATLAB R2017a (www.mathworks.com).

We examined associations between the six measured meteorological variables and RWA activity and CH_4 concentrations. As many of these variables were correlated with one another, we used principal components analysis (R function prcomp) on centred and scaled data to create composite "weather" variables (i.e., principal axes) that were used in subsequent analyses.

We used the "median + 2MAD" method [42] to separate true peaks in CH_4 concentrations from background or naturally-elevated concentrations: any observation greater than the overall median + 2MAD (2.31 ppm CH_4 in nest gas and 2.11 ppm CH_4 in ambient air) was considered a peak concentration. Background and elevated CH_4 concentrations were separated based on the 90% quantile of the CH_4 concentration [43]. For interpreting the significance of the correlation coefficient, we followed [44]. For δ^{13}C-CH_4, we considered concentrations < −35‰ or >0‰ to be peak concentrations. Only peaks occurring in both data sets at the same time were considered true peaks. The Keeling plot method, first invented in 1958 [45], is a graphical analysis method widely used in research into terrestrial ecosystems [46], paleoclimates [47], the terrestrial carbon cycle [48] or emissions along fault zones [10]. The Keeling plot relies on the assumption of mass conservation when carbon is exchanged between two reservoirs and allows for the quantification of the contributing processes when carbon is exchanged between a reservoir inside the Earth and the atmosphere [48]. The Keeling plot method [10,46] was applied to determine the carbon-isotope composition of the found peaks to obtain insights into the processes that govern the distinction between isotopes in the ecosystem.

2.8. Availability of Data

Data are available from the Harvard Forest Data Archive (http://harvardforest.fas.harvard.edu/data-archive), dataset HF305.

3. Results

3.1. Meteorological Conditions

During the one-week field campaign in August 2016, air temperatures ranged from 5.7–29.1 °C (mean = 16.2 °C), with only 2.1 mm rainfall that occurred overnight between 9 and 10 August. Variation in atmospheric pressure (mean 988 ± 2.24 hPa) and wind speed (1.67 ± 1.72 km/h) were small. The first three axes derived by the principal components analysis accounted for nearly 80% of the variance in the data (Table 1). The first axis represents temperature and humidity, the second axis represents atmospheric pressure (with additional contributions of humidity and windspeed), and the third axis represents rainfall and windspeed (with a minor contribution of temperature).

Table 1. Results of the principal components analysis of the measured weather variables. Values in the first six rows are the loadings of each variable on each of the first three principal axis (PC); only loadings > |0.3| are shown. The last row of the table gives the cumulative proportion of the variance explained by each of the first three principal axes.

Variable	PC-1	PC-2	PC-3
Temperature (°C)	−0.69		0.3
Atmospheric Pressure (hPa)		0.62	
Dew-point (°C)	−0.43	0.49	
Relative humidity (%)	0.48	0.45	
Rainfall (mm)			0.77
Windspeed (km/h)		−0.41	0.50
Cumulative variance explained	0.34	0.59	0.77

Median RWA activity and the three principal axes of weather were modestly associated, and accounted for only 8% of the variance in ant activity (Table 2). The ant activity increased slightly at lower temperatures (PC-1) and slightly decreased when rainfall (PC-3) was present. PC-2 was not associated significantly with RWA activity.

Table 2. Summary Analysis of Variance ANOVA table of the linear model examining the effects of weather conditions on median RWA activity. The estimate is the slope describing the relationship between each principal component and median RWA activity. The remaining columns are the degrees of freedom, mean square, and F-statistic for each term in the model. (*** $p < 0.001$; ^{NS} $p > 0.5$). Overall model $r^2 = 0.08$; $F_{3,1563} = 47.57$, $p < 0.001$.

Components	Estimate	Df	MS	F
PC-1	0.19	1	110.8	120.6 ***
PC-2	−0.01	1	0.3	0.3 ^{ns}
PC-3	−0.11	1	20.0	21.8 ***
Residual		1563	0.9	

Weather conditions explained 10% of the variation in CH_4 (ppm) (Table 3), but explained 22% of the variation in $\delta^{13}C$-CH_4 (‰), which decreased with all measured weather variables (Table 4).

Table 3. Summary ANOVA table of the linear model examining the effects of weather conditions on CH_4 concentration (ppm). The estimate is the slope describing the relationship between each principal component and CH_4 concentration. The remaining columns are the degrees of freedom, mean square, and F-statistic for each term in the model. (*** $p < 0.001$; * $p < 0.5$). Overall model $r^2 = 0.19$; $F_{3,1563} = 121.5$, $p < 0.001$.

Components	Estimate	Df	MS	F
PC-1	−0.3	1	263.1	323.8 ***
PC-2	0.1	1	29.8	36.6 ***
PC-3	0.04	1	3.4	4.1 *
Residual		1563	0.8	

Table 4. Summary ANOVA table of the linear model examining the effects of weather conditions on δ^{13}C-CH_4 (‰). The estimate is the slope describing the relationship between each principal component and CH_4 concentration. The remaining columns are the degrees of freedom, mean square, and F-statistic for each term in the model. (*** $p < 0.001$). Overall model $r^2 = 0.22$; $F_{3,1563} = 149.5$, $p < 0.001$.

Components	Estimate	Df	MS	F
PC-1	0.22	1	153.2	196.8 ***
PC-2	−0.24	1	137.8	177.0 ***
PC-3	−0.19	1	58.2	74.8 ***
Residual		1563	0.8	

3.2. RWA Activity

Ants were most active during the late afternoon and early evening hours (Figures 3a and 4a). The video streams showed that during the measurement period the ants continued to forage, build and maintain the nest. Decomposition of the time-series into its additive components (Figure 3b–d) illustrated that during the one-week gas-sampling campaign, there was a trend towards increasing activity over the first four days, followed by a sharp decline towards the end of the week (Figure 3b). There were two noticeable peaks of activity, at mid-day and early afternoon, followed by sharp spikes in activity near 16:30 h (Figure 3c). No nuptial flights happened during this week.

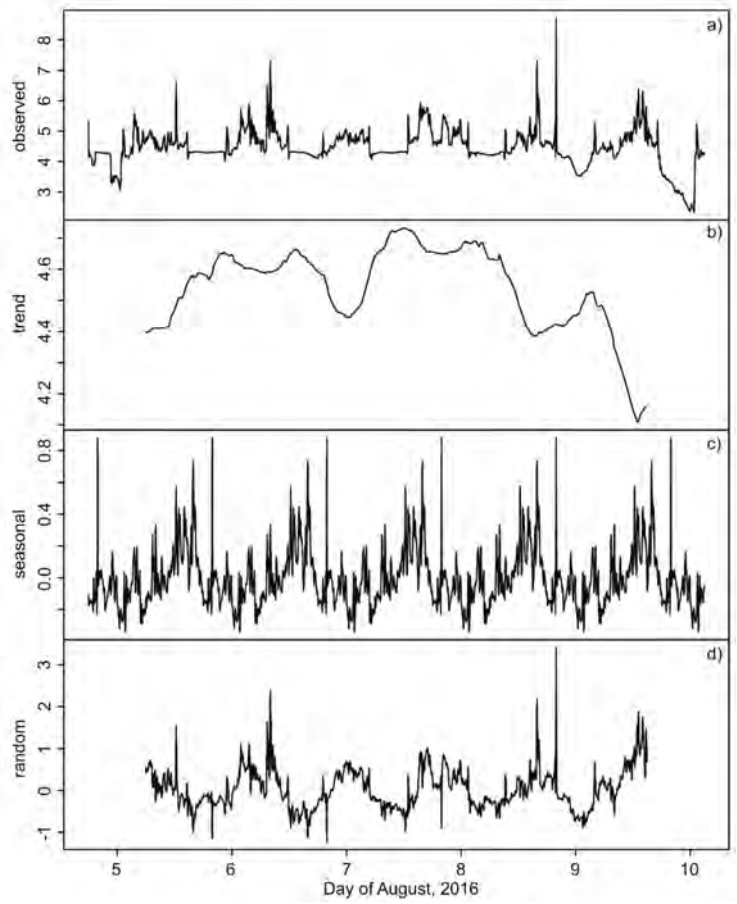

Figure 3. Additive time-series decomposition of median RWA activity. An extreme spike in ant activity (observed = 12 units on 4 August at 19:14 UTC and 25 units on 4 August at 19:19 UTC) are not shown to enhance clarity of the "observed" time-series. The observed data (**a**) can be partitioned (additively decomposed) into its temporal trend estimated by a polynomial smoothing function (**b**); a daily ("seasonal") cycle (**c**); and residual (random) variation (**d**).

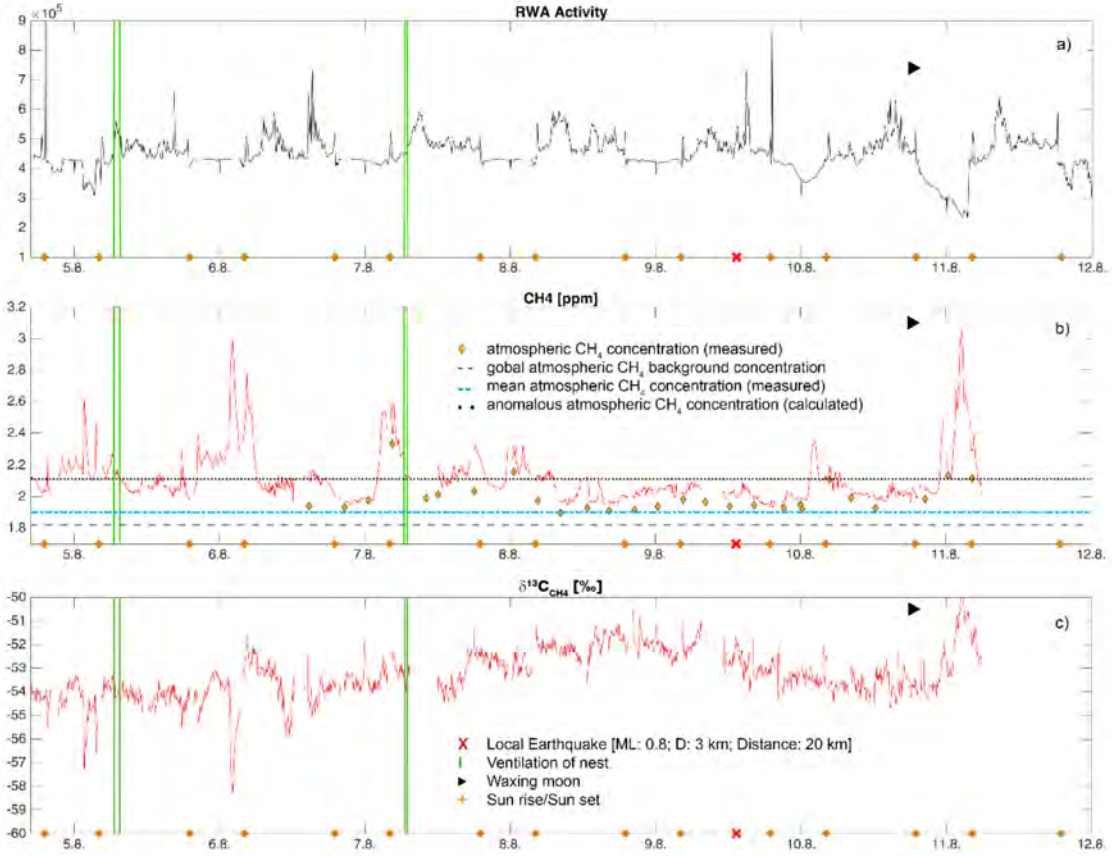

Figure 4. Time-series plots of median RWA activities (**a**), CH_4 (**b**), and δ^{13}C-CH_4 (**c**) in nest gas. Green lines indicate ventilation phases of the nest, orange crosses sunrise/sunset, and a red cross a single local earthquake. Reference lines indicate the global atmospheric CH_4 background concentration ([3]; black dashed line), the local mean CH_4 atmospheric concentration (blue dotted line), and the calculated anomalous atmospheric CH_4 concentration (black dotted line) during the sampling week in August 2016.

Additional external agents that may have influenced RWA activity were visually assessed; ventilation phases of the nest took place in the early morning (6:40–7:30 UTC) on 5 August for 50 min and on 7 August for 20 min (6:40–7:00 UTC) after sunrise with varying ant activities (Figure 4a). On two days (7 August and 9 August), at 04:30 and 05:50 (UTC), respectively, golden hammer birds (*Emberiza citronella*) were "anting" for ≈5 min to kill parasites on their feathers with formic acid; a mouse was observed on the nest at 22:00 (UTC) for 10 min on 4 August 2016. These biotic effects did not appear to influence any RWA activity.

3.3. CH_4 and δ^{13}C-CH_4 in Nest Gas

A total of 459,704 data points were collected during the 192-h sampling period for each of CH_4 and δ^{13}C-CH_4. Concentrations of CH_4 in the nest exceeded the global atmospheric background concentration (1.82 ppm [3]) and ranged from 1.93 to 3.07 ppm (Figure 4b, Table 5). Atmospheric CH_4 concentrations were slightly variable (1.90–2.33 ppm). The calculated anomalous threshold concentration after [42] for atmospheric CH_4 was 2.11 ppm CH_4 (Figure 4b). In ambient air, only four measurements out of 27 exceeded this threshold. In nest gas, the anomalous threshold was 2.31 ppm CH_4. To compare our findings to fault-related emissions [10], the 90th percentile of CH_4 was estimated. In nest gas, 10% of measured CH_4 was larger than the 90th percentile (Table 5). Nest gas concentrations of CH_4 appear to result from fault-related emissions moving via fault networks through the RWA nest.

A comparison with fugitive emissions of CH_4 (ppm) from basin bounding faults in the UK [10]; Table 5 showed that mean nest gas emissions are of the same order, although we had 20× more observations.

Table 5. Descriptive statistics for nest gas CH_4 (ppm) at the Goloring site compared to fugitive emissions of CH_4 (ppm) from basin bounding faults in the UK [10]. SE = 1 standard error of the mean.

Data Amount	Location	Target	N	Mean	SE	Min	Max
All data	Widmerpool	Fault	8313	1.91	0.000395	1.89	2.80
	Lancashire	Fault	5568	1.88	0.00041	1.87	3.18
	Butterknowle	Fault	9283	1.87	0.000342	1.86	3.97
	90 Fathom	Fault landfill	9374	2.24	0.0151	1.86	13.73
	90 Fathom	Fault no landfill	8537	1.89	0.000452	1.86	2.52
	Vale of Eden	Fault	8428	2.20	0.00169	1.87	4.88
This Study	Goloring site	Nest gas	459,704	2.13	0.000238	1.93	3.07
Data > 90th percentile	Widmerpool	Fault	5	2.34	0.0579	2.24	2.56
	Lancashire	Fault	6	2.56	0.139	2.32	3.18
	Butterknowle	Fault	3	2.34	0.0233	2.29	2.36
	90 Fathom	Fault landfill	692	5.74	0.119	13.73	13.73
	90 Fathom	Fault no landfill	11	2.25	0.0101	2.31	2.31
	Vale of Eden	Fault	2234	2.32	0.00188	2.22	3.23
This Study	Goloring site	Nest gas	47,147	2.50	0.00079	2.32	3.07

δ^{13}C-CH_4 in the nest ranged from −58.48 to −49.54‰ (Figure 4c). Eight significant peaks (red and blue marks in Figure 5a,b) in nest gas were found for CH_4 and δ^{13}C-CH_4 (Figure 5a,b). These peaks occurred between 17:39 (UTC) and 06:54 (UTC) the following day, but were otherwise not temporally predictable. Results of the Keeling plots [46] revealed two signatures for δ^{13}C-CH_4 at −37‰ (blue markers and dots in Figure 5a–c) and −69‰ (red markers and dots in in Figure 5a–c) in nest gas (Figure 5c).

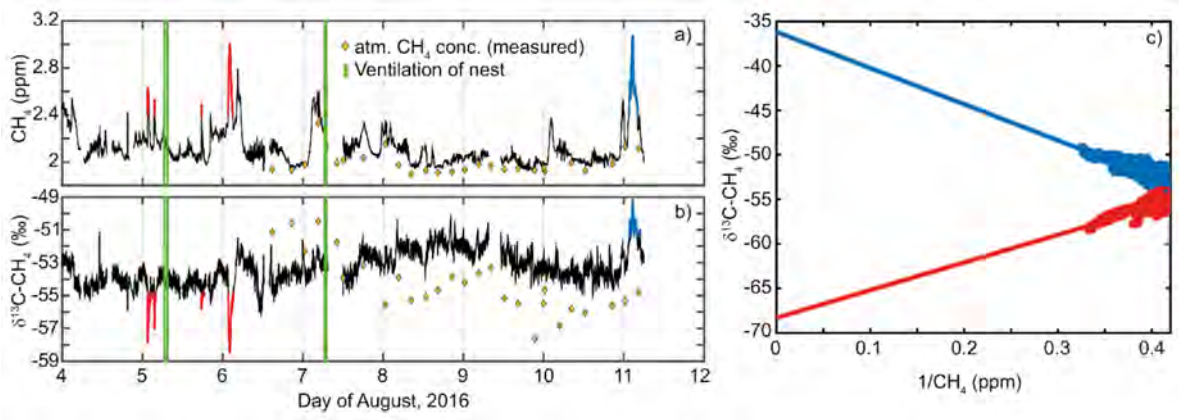

Figure 5. CH_4 (**a**), δ^{13}C-CH_4 (**b**) peak concentrations and Keeling plot of δ^{13}C-CH_4 (**c**) from nest gas. Note the peaks indicate two signatures for δ^{13}C-CH_4 in nest gas at −37‰ and −69‰ (**c**). For better identification of the signatures in the Keeling plot, peak concentrations in CH_4 and δ^{13}C-CH_4 were colored in (**a**,**b**). Red signatures in the Keeling plot refer to the marked red peak concentrations in (**a**,**b**), whereas blue signatures in the Keeling plot to the marked blue peak concentrations in (**a**,**b**).

Joint visualization of the time series of ant activity, methane concentrations, and weather (Figure 6a) reveal that all the time series exhibited a periodicity of approximately 24 h. Cross-correlations showed positive and negative peaks at daily intervals (Figure 6b). The absolute value of the cross-correlation coefficient ≤0.3, and the strongest cross-correlation occurred at a lag of ≈−30 min, less than the original filter width of the ant activity time series.

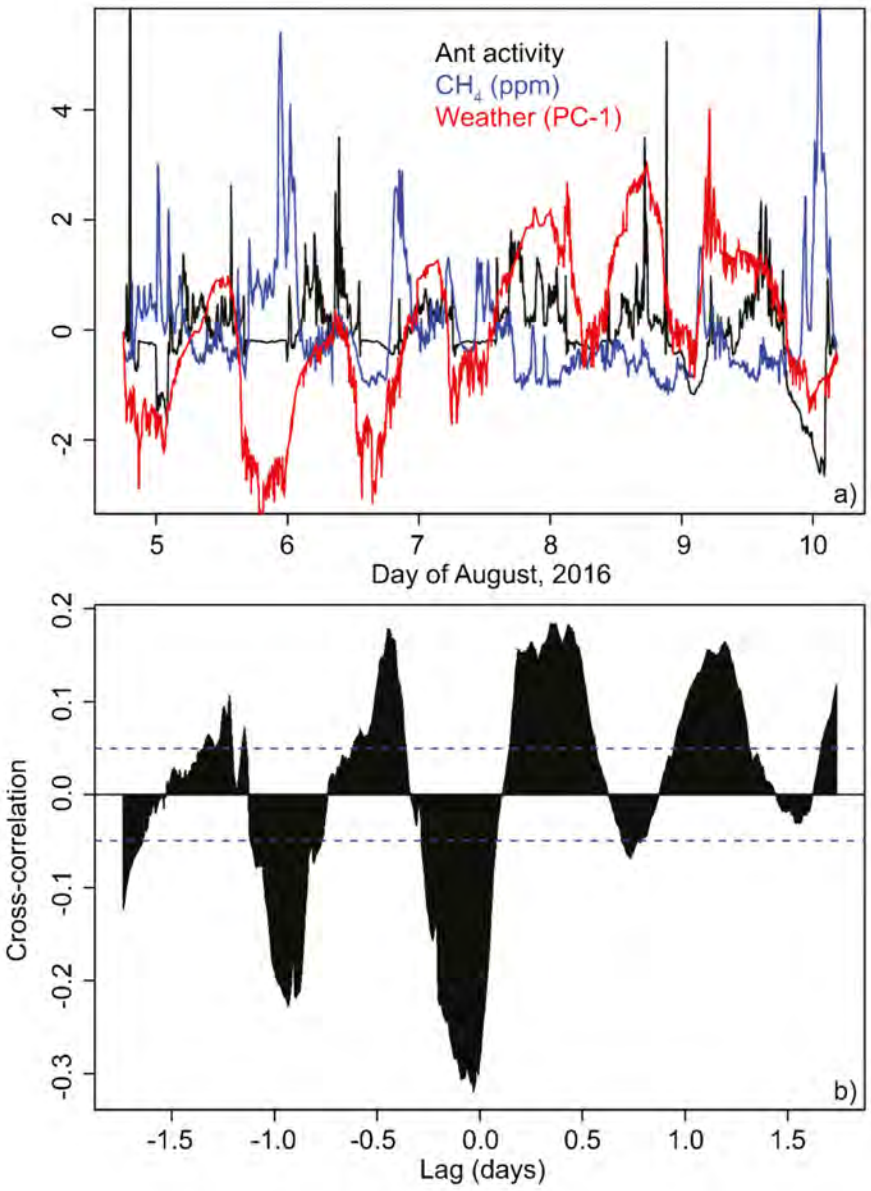

Figure 6. Relationships between ant activity, CH_4 and weather conditions. Time-series plots of (**a**) median ant activity (black), methane concentration in the nest (blue), and weather conditions (PC-1, red). Cross-correlation (**b**) between median ant activity and methane degassing. All values are centered and scaled (i.e., are reported in SD units).

3.4. Earth Tides and Earthquakes

Earth tides were basically semi-diurnal. Methane activity (Figure 7a,b) showed a low negative correlation with earth tides of ≈ -0.4 at a lag of 6–8 h. The cross-correlation between the earth tides and δ^{13}C-CH_4 was $\leq |0.15|$ (Figure 7c). Only one earthquake [35,40] occurred nearby (local magnitude: 0.8; depth: 3 km; distance: 20 km; Figure 4). This micro-earthquake neither influenced degassing nor RWA activity.

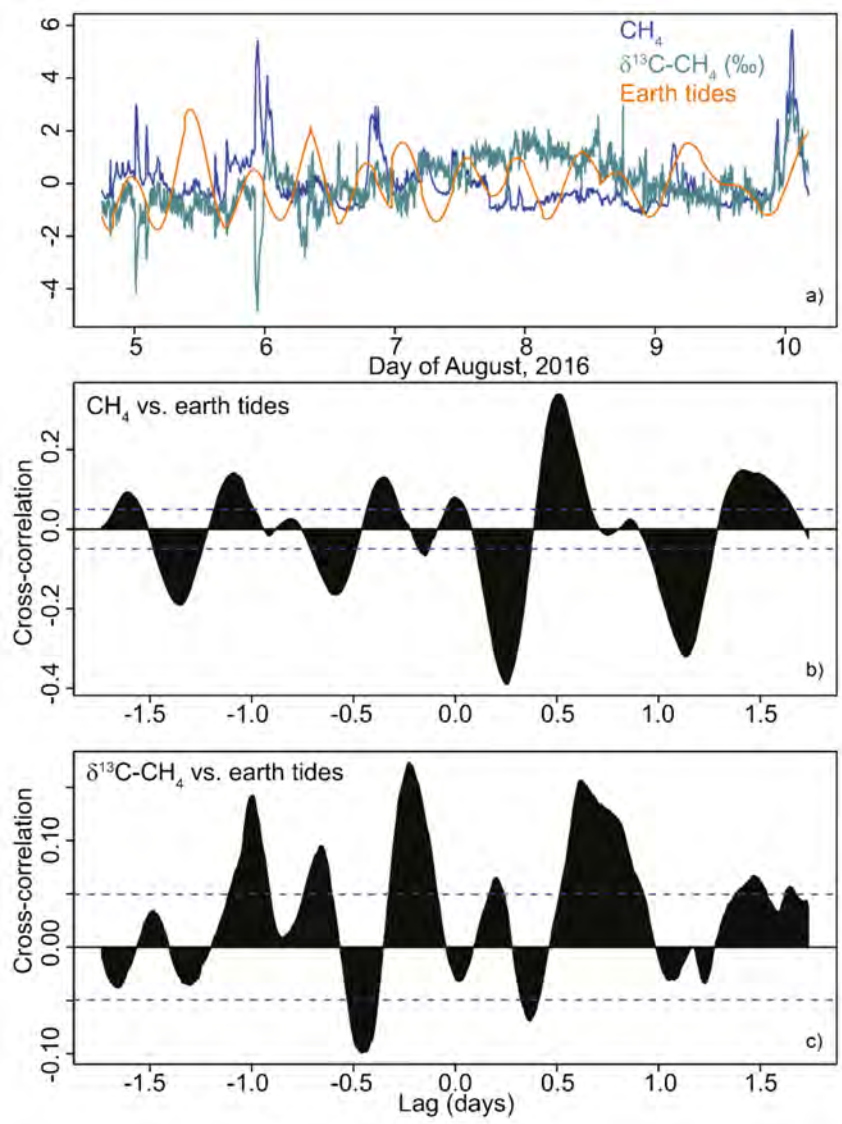

Figure 7. Relationships between nest CH_4 (blue), $\delta^{13}C$-CH_4 (green), and earth tides (orange). Time-series (**a**) of centered and scaled data. Cross-correlation of the time-series of CH_4 (**b**) and $\delta^{13}C$-CH_4 (**c**) with earth tides.

4. Discussion

Our results provide for the first time a continuous in-situ record of both CH_4 and $\delta^{13}C$-CH_4 in a RWA nest. Although our results of CH_4 and $\delta^{13}C$-CH_4 in nest gas may not be representative of these values for the entire year, the measurement data provide a continuous set of observations of multiple variables matched in time, in contrast to other data reported in literature for which different nests were sampled at different times (two days) and CH_4 flux was estimated in laboratory incubations from samples of nest material [6].

4.1. CH_4 and $\delta^{13}C$-CH_4 in Nest Gas

Results from our short (192-h) but continuous in-situ sampling confirmed our 1st hypothesis that elevated CH_4 concentrations in nest gas appear to result from fault-related emission moving via fault networks through the RWA nest. In contrast to [21], our results also show that a red wood ant nest acts as a CH_4 source. Bender and Wood [22] attribute nest gas CH_4 to high NH_4-N concentrations in ant mounds. A comparison of our results with data on fugitive emissions of CH_4 (ppm) from basin

bounding faults in the UK (Boothroyd et al. 2017; Table 5) showed that mean nest gas emissions are of the same order. Elevated CH_4 concentrations in nest gas appear to result from a combination of microbial activity and fault-related emissions moving via through fault networks through the RWA nest, because in most geologic environments biotic and abiotic gases are mixed [2].

Comparison of δ^{13}C-CH_4 nest-gas signatures with published data suggests that CH_4 in the ant nest can be attributed to two different sources (Figure 8). The δ^{13}C-CH_4 signature of -69‰ in nest gas indicates a microbial source, such as decomposing organic matter that is high in nutrients [8]. This result supports the findings of [22] that the aboveground parts of ant nests are hot-spots of CH_4 production.

The second isotope signature, -37‰ δ^{13}C-CH_4, likely is fault-related, and can be attributed either to thermogenic [10] or to abiotic CH_4 formation [49]. Boothroyd et al. [10] found a δ^{13}C-CH_4 signature of -37‰ for fugitive emission of CH_4 via migration along fault zones in the United Kingdom. Our result of -37‰ δ^{13}C-CH_4 is of the same order (Figure 8) and can be attributed to fault-related CH_4 emission moving through the RWA nest. This result also provides the first evidence that RWA nests may be associated with fault-related emissions of CH_4.

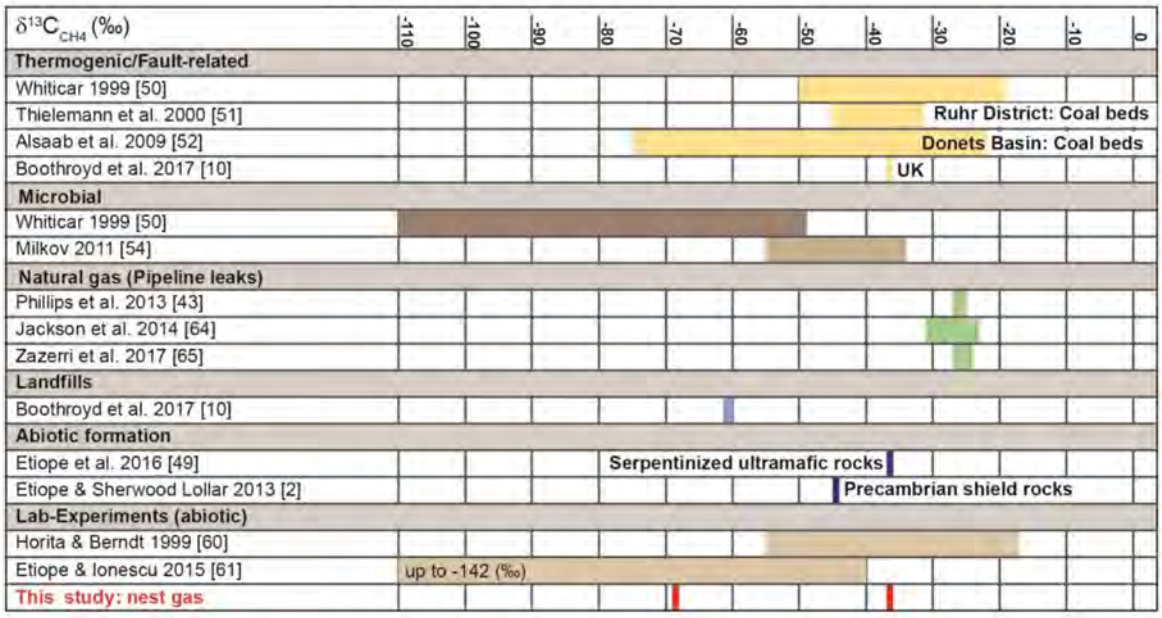

Figure 8. Comparison of δ^{13}C-CH_4 in nest gas signatures to published data. The two nest-gas signatures indicate a microbial source and a thermogenic or abiotic fault-related one.

Continental loss of volatiles requires tectonically active parts and the formation of fluid-filled conduits through the continental crust. Suitable locations can be found in extensional regimes and their related volcanism [30], such as are present in our study area. Gas permeable faults and fractured rocks are pathways to naturally release significant amounts of "old" CH_4 of crustal origin. Significant geologic CH_4 emissions, comprising both biogenic and thermogenic CH4, result from hydrocarbon production in sedimentary basins and, subordinately, to inorganic Fischer-Tropsch-type reactions occurring in geothermal systems [24]. A variety of geological, chemical and biological processes have impacts on the deep carbon cycle. There are three possible sources for the fault-related CH_4 we find in RWA nests.

First, carboniferous coals are sources of thermogenic coalbed methane (CBM) in numerous basins, including the Ruhr and Donets Basins. Their ^{13}C are values between -20‰ and -75‰ ([50–52]; Figure 8). Both basins have coal thicknesses of ≈100 m [52,53]. Additionally, secondary microbial methane can be formed during petroleum biodegradation in conventional reservoirs ([54]; Figure 8). In our study area, Devonian coal seams with very small thicknesses [26] are reported at depths up to

9000 m, which are much older than the Ruhr and Donets Basins. Though the study area is situated in a suitable tectonic compression/extensional regime, any thermogenic CH_4 likely would be small because of the very low thickness of the seams and might not even lead to measurable coal-bed CH_4 concentrations in nest gas. On the other hand, lignite and coal formations are often associated with aerobic methylotrophs at depths of over 1 km and are usually considered to be anaerobic [55–57]. In the study area, several small lignite seams (Middle to Upper Eocene) with a thickness of up to 5 m are found in depths of ≈75–160 m. The low thickness and the shallow depth of the lignite may not lead to thermogenic CH_4 seepage. Furthermore, secondary microbial methane formation can be excluded because no petroleum or oil formation is reported in our study area [26] and coal and petroleum/oil formation ("oil window") have different formation histories [58,59].

Second, δ^{13}C-CH_4 in land-based serpentinized ultramafic rocks can be as light as −37‰, and methane from Precambrian shields may exhibit even lower values (−45‰) [2,4,45]. Laboratory experiments have produced abiotic methane with a wide range of δ^{13}C-CH_4 signatures, including isotopically "light" values once thought to be indicative of biological activity (e.g., −19 to −53.6‰ by [60]; −41 to −142‰ by [61]). Abiotic CH_4 can be mistaken for biotic CH_4 of microbial or thermogenic origin because minor amounts of abiotic gas in biotic gas may prevent its recognition based on C and H isotope analysis [49,62]. Sources of abiotic CH_4 formation in the study area can be attributed to magmatic CH_4 formation due to late magmatic (<600 °C) re-distribution of C-O-H fluids during magma cooling or gas-water-rock-interactions even at low temperatures and pressures [2]. In the study area, the magmatic source for magmatic CH_4 formation could be the so called "Eifel plume", a region of about 100–120 km in diameter between 50–60 km depth and at least 410 km depth beneath the study area. The buoyant Eifel plume is characterized by excess temperature of 100–150 K, has approx. 1% of partial melt and is the main source of regional Quaternary volcanism [63].

Third, gas-water-rock-interactions, including dissolution of C- and Fe-bearing minerals in water at ~300 °C and carbonate methanation between 250 and 800 °C, do not depend on magma or magma-derived fluids [2,5]. The "Klerf Schichten" (Lower Ems) are alternating layers of reddish Fe-bearing sandstones and C-bearing shales and schists ≤2200-m thick and may be suitable formations for decomposition of C- and Fe-bearing minerals [26]. Paleozoic bedrock sediments, especially the "Sphaerosiderith Schiefer" (Upper Ems; ≤150-m thick) schists with iron concretions ("Eisengallen"), are suitable formations for carbonate methanation: the decomposition of carbonate minerals (calcite, magnesite, siderite) at lower temperatures in H_2-rich environments without mediation of gaseous CO_2 (as is usually the case for catalytic hydrogenation or FTT reaction) [2,26]. Within the habitable zone in the upper crust, at temperatures >150 °C and in the presence of CO_2, CO, and H_2, CH_4 may be produced in aqueous solution even in the absence of a heterogeneous catalyst or gas phase by a series of redox reactions leading to the formation of formic acid, formaldehyde and methanol. Finally, abiotic CH_4 can also form in situ through low temperature processes including the Sabatier and Fischer-Tropsch type (FTT) synthesis reactions with metals like Fe or Ni or clay minerals as catalysts [2,5].

Because the largest quantities of abiotic gases found on Earth's surface are produced by low-temperature gas–water–rock reactions [61] we attribute the −37‰ δ^{13}C-CH_4 signature in RWA nests to fault-related emissions of abiotically formed CH_4 by gas-water-rock reactions occurring at low-temperatures in a continental setting at shallow depths (micro-seepage; [61]). Probable sources include Devonian schists ("Sphaerosiderith Schiefer") with iron concretions ("Eisengallen") sandstones or the iron-bearing "Klerf Schichten" [26]. However, we cannot exclude the possibility of overlap by magmatic CH_4 micro-seepage from the Eifel plume [27].

Furthermore, our results show no relation to pipeline leaks of natural gas [43,64,65].

In summary, we suggest that RWA nests are associated with actively degassing faults from the deep underground. Given the abundance of RWA nests on the landscape, their role as sources of microbial CH_4 and biological indicators for abiotically-derived CH_4 should be included in estimations of methane emissions that are contributing to climatic change. The corresponding author has already mapped more than 25,000 red wood ant nests by herself together with co-author Martin B. Berberich in

distinct locations of Germany. Projected onto the entirety of Germany there might be some hundreds of thousands of red wood ant nests. Inferring this figure to the entirety of environments (Eurasia, North America, Canada) where red wood ant nests are known and mapped, their large number suggests their relevance as a source of microbial CH_4 and will have an influence on the global carbon cycle.

Furthermore, future work should investigate more RWA nests, of both *F. polyctena* and other RWA species, to determine if the −37‰ signature can be attributed to a purely abiotic source, or a combination of abiotic and thermogenic sources. Such a study should use additional measurements of ^{13}H and run long enough to determine the influence of irregularly timed earthquake events on patterns of methane degassing.

4.2. Earth Tides and Earthquakes

Neither the earth tides nor the micro-earthquake influenced degassing nor RWA activity.

4.3. RWA Activities and External Parameters

Neither our second or third hypotheses were supported by the data. During the investigation period, ant activity was higher than we had observed in 2009–2012, although an "M-shaped" pattern in daily activity was still identifiable [36]. Relatively high RWA activities during the late afternoon and early evening hours could be attributable to direct sun hitting the nest during that time or with activities associated with rebuilding damage to the nest. We did not find any evidence that ant activity changed during the CH_4 (micro)-seepage process, or that there were external effects of weather (see also [36]), or methane seepage. Additional external agents, including mice and "anting" birds, or micro-earthquakes, did not influence ant activities during the sampling week. We conclude that during our 8-day sampling period, RWA activity was independent from external parameters.

4.4. Nest Gas CH_4 and $\delta^{13}C$-CH_4 and External Parameters

We also did not find strong support for a relationship between CH_4 in the nest and external variables during our 8-day sampling period. Atmospheric CH_4 concentrations were always lower than CH_4 in the RWA nest and there seemed to be little influence of atmospheric CH_4 on CH_4 in the nest. Less than 25% of the variance in CH_4 and $\delta^{13}C$-CH_4 was accounted for by weather conditions (cf. [66]). Earth tides also were not correlated with methane degassing in the nest. The −37‰ $\delta^{13}C$-CH_4 signature in nest gas was detected only once. The micro-earthquake on 9 August did not influence CH_4 degassing because of its far distance (20 km). On 13 August, there was another earthquake (ML: 0.7; D = 13 km) only 2.3 km away from the nest. It might be that the −37‰ $\delta^{13}C$-CH_4 signature in nest gas was a precursor to the 13 August earthquake, promoting degassing due to an increase in compressive stress [9,10]. But this remains unanswered as the CH_4 measurement campaign was terminated on 11 August.

5. Conclusions

For the first time, both CH_4 and fault-related $\delta^{13}C$-CH_4 in a RWA nest was continuously recorded in situ. Neither methane degassing nor RWA activity was synchronized with earth tides, micro-earthquakes, or weather conditions. Elevated CH_4 concentrations in nest gas appear to result from a combination of microbial activity and fault-related emissions moving via through fault networks through the RWA nest. Two $\delta^{13}C$-CH_4 signatures were identified in nest gas: −69‰ and −37‰. The −69‰ signature of $\delta^{13}C$-CH_4 within the RWA nest is best attributed to microbial decomposition of organic matter. This finding supports previous findings that RWA nests are hot-spots of microbial CH_4. Additionally, the −37‰ $\delta^{13}C$-CH_4 signature is the first evidence that RWA nests also may be associated with fault-related emissions of CH_4. The −37‰ $\delta^{13}C$-CH_4 signature can be attributed either to fault-related thermogenic or abiotic CH_4 formation originating from, for example, low-temperature gas-water-rock reactions in a continental setting at shallow depths (micro-seepage). Future work on

the −37‰ signature should investigate more RWA nests, additional species of RWA, use additional measurements of ^{13}H, and run long enough to determine the influence of irregularly timed earthquake events on patterns of methane degassing.

Acknowledgments: The study is part of the research project "GeoBio-Interactions" funded by the VW-Stiftung (grant number Az 93 403) within the initiative "Experiment!"—Auf der Suche nach gewagten Forschungsideen. The VW-Stiftung had no role in the design of the study; in the collection, analyses, or interpretation of data; in the writing of the manuscript, and in the decision to publish the results. We thank Daniela Polag and Jan Hartmann (University of Heidelberg) for doing the nest-gas sampling. RWA activity recording was done using equipment from the Department of Geology at University of Duisburg-Essen. We also thank Dr. Peter Henrich (Leiter der Direktion Landesarchäologie—Außenstelle Koblenz) for his permission to conduct the survey on the Goloring site, and Hans-Toni Dickers, Paul Görgen and Bernd Klug from Kuratorium für Heimatforschung und -pflege, Kobern-Gondorf for their support during the field campaign.

Author Contributions: Gabriele M. Berberich conceived the idea, collected the data, carried out the statistical analysis and wrote the manuscript. Aaron M. Ellison carried out the statistical analysis and edited the manuscript. Martin B. Berberich collected the data, carried out the statistical analysis and contributed to the manuscript. Arne Grumpe, Adrian Becker and Christian Wöhler further developed the automated image analysis routine and contributed to the manuscript.

Conflicts of Interest: The authors declare no conflict of interest.

References

1. Keppler, F.; Boros, M.; Frankenberg, C.; Lelieveld, J.; McLeod, A.; Pirttilä, A.M.; Pirttilä, A.M.; Röckmann, T.; Schnitzler, J.P. Methane formation in aerobic environments. *Environ. Chem.* **2009**, *6*, 459–465. [CrossRef]
2. Etiope, G.; Sherwood Lollar, B. Abiotic methane on earth. *Rev. Geophys.* **2013**, *51*, 276–299. [CrossRef]
3. Saunois, M.; Bousquet, P.; Poulter, B.; Peregon, A.; Ciais, P.; Canadell, J.G.; Dlugokencky, E.J.; Etiope, G.; Bastviken, D.; Houweling, S.; et al. The Global Methane Budget: 2000–2012. *Earth Syst. Sci. Data* **2016**, *8*, 697–751. [CrossRef]
4. Etiope, G.; Schoell, M. Abiotic gas: Atypical, but not rare. *Elements* **2014**, *10*, 291–296. [CrossRef]
5. Kiätävienen, R.; Purkamo, L. The origin, source, and cycling of methane in deep crystalline rock biosphere. *Front. Microbiol.* **2015**, *6*, 725. [CrossRef] [PubMed]
6. Jílková, V.; Picek, T.; Šestauberová, M.; Krištůfek, V.; Cajthaml, T.; Frouz, J. Methane and carbon dioxide flux in the profile of wood ant (*Formica aquilonia*) nests and the surrounding forest floor during a laboratory incubation. *FEMS Microbiol. Ecol.* **2016**, *92*, fiw141. [CrossRef] [PubMed]
7. Schoell, M. The hydrogen and carbon isotopic composition of methane from natural gases of various origins. *Geochim. Cosmochim. Acta* **1980**, *44*, 649–661. [CrossRef]
8. Keppler, F.; Hamilton, J.T.G.; Bra, M.; Röckmann, T. Methane emissions from terrestrial plants under aerobic conditions. *Nature* **2006**, *439*, 187–191. [CrossRef] [PubMed]
9. Birdsell, D.T.; Rajaram, H.; Dempsey, D.; Viswanathan, H.S. Hydraulic fracturing fluid migration in the subsurface: A review and expanded modeling results. *Water Resour. Res.* **2015**, *51*, 7159–7188. [CrossRef]
10. Boothroyd, I.M.; Almond, S.; Worrall, F.; Davies, R.J. Assessing the fugitive emission of CH_4 via migration along fault zones—Comparing potential shale gas basins to non-shale basins in the UK. *STOTEN* **2017**, *580*, 412–424. [CrossRef]
11. Ciotoli, G.; Lombardi, S.; Zarlenga, F. Natural leakage of helium from Italian sedimentary basins of the Adriatic structural margin. Perspectives for geological sequestration of carbon dioxide. In *Advances in the Geological Storage of Carbon Dioxide*; Springer Science & Business Media: Berlin, Germany, 2006; pp. 191–202.
12. Etiope, G. Natural emissions of methane from geological seepage in Europe. *Atmos. Environ.* **2009**, *43*, 1430–1443. [CrossRef]
13. Berberich, G. Identifikation Junger Gasführender Störungszonen in der West- und Hocheifel mit Hilfe von Bioindikatoren. Ph.D. Thesis, University of Duisburg-Essen, Duisburg, Germany, 2010.
14. Berberich, G.; Schreiber, U. GeoBioScience: Red Wood Ants as Bioindicators for Active Tectonic Fault Systems in the West Eifel (Germany). *Animals* **2013**, *3*, 475–498. [CrossRef] [PubMed]
15. Berberich, G.; Grumpe, A.; Berberich, M.; Klimetzek, D.; Wöhler, C. Are red wood ants (Formica rufa-group) tectonic indicators? A statistical approach. *Ecol. Ind.* **2016**, *61*, 968–979. [CrossRef]

16. Del Toro, I.; Berberich, G.M.; Ribbons, R.R.; Berberich, M.B.; Sanders, N.J.; Ellison, A.M. Nests of red wood ants (*Formica rufa*-group) are positively associated with tectonic faults: A double-blind test. *PeerJ* **2017**, *5*, e3903. [CrossRef] [PubMed]
17. Risch, A.C.; Jurgensen, M.F.; Schütz, M.; Page-Dumroese, D.S. The contribution of red wood ants to soil C and N pools and CO_2 emissions in subalpine forests. *Ecology* **2005**, *86*, 419–430. [CrossRef]
18. Risch, A.C.; Schütz, M.; Jurgensen, M.F.; Domisch, T.; Ohashi, M.; Finér, L. CO_2 emissions from red wood ant (*Formica rufa* group) mounds: Seasonal and diurnal patterns related to air temperature. *Ann. Zool. Fennici* **2005**, *42*, 283–290.
19. Ohashi, M.; Finér, L.; Domisch, T.; Risch, A.C.; Jurgensen, M.F. CO_2 efflux from a red wood ant mound in a boreal forest. *Agric. For. Meteorol.* **2005**, *30*, 131–136. [CrossRef]
20. Ohashi, M.; Finér, L.; Domisch, T.; Risch, A.C.; Jurgensen, M.F.; Niemelä, P. Seasonal and diurnal CO_2 efflux from red wood ant (*Formica aquilonia*) mounds in boreal coniferous forests. *Soil Biol. Biochem.* **2007**, *39*, 1504–1511. [CrossRef]
21. Wu, H.; Lu, X.; Wu, D.; Song, L.; Yan, X.; Liu, J. Ant mounds alter spatial and temporal patterns of CO_2, CH_4 and N_2O emissions from a marsh soil. *Soil Biol. Biochem.* **2013**, *57*, 884–891. [CrossRef]
22. Bender, M.R.; Wood, C.W. Influence of red imported fire ants on greenhouse gas emissions from a piedmont plateau pasture. *Commun. Soil Sci. Plant Anal.* **2003**, *34*, 1873–1889. [CrossRef]
23. Crockett, R.G.M.; Perrier, F.; Richon, P. Spectral-decomposition techniques for the identification of periodic and anomalous phenomena in radon time-series. *Nat. Hazards Earth Syst. Sci.* **2010**, *10*, 559–564. [CrossRef]
24. Etiope, G.; Klusman, R.W. Geologic emissions of methane to the atmosphere. *Chemosphere* **2002**, *49*, 777–789. [CrossRef]
25. Litt, T.; Brauer, A.; Goslar, T.; Merk, J.; Balaga, K.; Mueller, H.; Ralska-Jasiewiczowa, M.; Stebich, M.; Negendank, J.F. Correlation and synchronisation of Lateglacial continental sequences in northern Central Europe based on annually laminated lacustrine sediments. *Quat. Sci. Rev.* **2001**, *20*, 1233–1249. [CrossRef]
26. LGB RLP. *Geologie von Rheinland-Pfalz*; Schweizbart'sche Verlagsbuchhandlung (Nägele u. Obermiller): Stuttgart, Germany, 2005; pp. 1–400. ISBN 3-510-65215-0. (In German)
27. Ritter, J.R.R.; Jordan, M.; Christensen, U.; Achauer, U. A mantle plume below the Eifel volcanic fields, Germany. *Earth Planet. Sci. Lett.* **2001**, *186*, 7–14. [CrossRef]
28. Walker, K.T.; Bokelmann, G.H.R.; Klemperer, S.L.; Bock, G. Shear-wave splitting around the Eifel hotspot: Evidence for a mantle upwelling. *Geophys. J. Int.* **2005**, *163*, 962–980. [CrossRef]
29. Tesauro, M.; Hollenstein, C.; Egli, R.; Geiger, A.; Kahle, H.G. Analysis of central western Europe deformation using GPS and seismic data. *J. Geodyn.* **2006**, *42*, 194–209. [CrossRef]
30. Clauser, C.; Griesshaber, E.; Neugebauer, H.J. Decoupled thermal and mantle helium anomalies: Implications for the transport regime in continental rift zones. *J. Geophys. Res.* **2002**, *107*, 2269. [CrossRef]
31. Hinzen, K.G. Stress field in the Northern Rhine area, Central Europe, from earthquake fault plane solutions. *Tectonophysics* **2003**, *377*, 325–356. [CrossRef]
32. Dèzes, P.; Schmid, S.M.; Ziegler, P.A. Evolution of the European Cenozoic Rift System: Interaction of the Alpine and Pyrenean orogens with their foreland lithosphere. *Tectonophysics* **2004**, *389*, 1–133. [CrossRef]
33. Ahorner, L. Historical seismicity and present-day microearthquake activity in the Rhenish Massif, Central Europe. In *Plateau Uplift: The Rhenish Shield—A Case History*; Fuchs, K., von Gehlen, K., Mälzer, H., Murawski, H., Semmel, A., Eds.; Springer: Berlin, Germany, 1983; pp. 198–221.
34. Ziegler, P.A.; Dèzes, P. Crustal Evolution of Western and Central Europe. In *European Lithosphere Dynamics*; Gee, D.G., Stephenson, R.A., Eds.; Geological Society of London: London, UK, 2006.
35. BNS—Erdbebenstation Bensberg. Available online: www.seismo.uni-koeln.de/catalog/index.htm (accessed on 1 September 2016).
36. Berberich, G.; Berberich, M.; Grumpe, A.; Wöhler, C.; Schreiber, U. First Results of 2.5 Year Monitoring of Red Wood Ants' Behavioural Changes and Their Possible Correlation with Earthquake Events. *Animals* **2013**, *3*, 63–84. [CrossRef] [PubMed]
37. Maes, F.; Collignon, A.; Vandermeulen, D.; Marchal, G.; Suetens, P. Multimodality image registration by maximization of mutual information. *IEEE Trans. Med. Imaging* **1997**, *16*, 187–198. [CrossRef] [PubMed]
38. Hinkle, M.E. Environmental conditions affecting concentrations of He, CO_2, O_2, and N_2 in soil gases. *Appl. Geochem.* **1994**, *9*, 53–63. [CrossRef]

39. Milbert, D. Solid Earth Tide. Version 15.02.2016. 2016. Available online: http://geodesyworld.github.io/SOFTS/solid.htm (accessed on 15 February 2016).
40. LGB RLP. Erdbebenereignisse Lokal. Aktuelle Erdbebenereignisse in Rheinland-Pfalz, Baden-Württemberg und in 1000 km Entfernung. Landeserdbebendienst Rheinland-Pfalz. Available online: http://www.lgb-rlp.de/fachthemen-des-amtes/landeserdbebendienst-rheinland-pfalz/ (accessed on 1 September 2016). (In German)
41. Kristan, M.; Leonardis, A.; Skočaj, D. Multivariate online kernel density estimation with Gaussian kernels. *Pattern Recognit.* **2011**, *44*, 2630–2642. [CrossRef]
42. Reimann, C.; Filzmoser, P.; Garrett, R.G. Background and threshold: Critical comparison of methods of determination. *Sci. Total Environ.* **2005**, *346*, 1–16. [CrossRef] [PubMed]
43. Phillips, N.G.; Ackley, R.; Crosson, E.R.; Down, A.; Hutyra, L.R.; Brondfield, M.; Karr, J.D.; Zhao, K.G.; Jackson, R.B. Mapping urban pipeline leaks: Methane leaks across Boston. *Environ. Pollut.* **2013**, *73*, 1–4. [CrossRef] [PubMed]
44. Hinkle, D.E.; Wiersma, W.; Jurs, S.G. *Applied Statistics for the Behavioral Sciences*, 5th ed.; Wadsworth Publishing: Belmont, CA, USA, 2009.
45. Keeling, C.D. The concentration and isotopic abundance of carbon dioxide in rural areas, Geochim. *Cosmochim. Acta* **1958**, *13*, 322–334. [CrossRef]
46. Pataki, D.E.; Ehleringer, J.R.; Flanagan, L.B.; Yakir, D.; Bowling, D.R.; Still, C.J.; Buchmann, N.; Kaplan, J.O.; Berry, J.A. The application and interpretation of Keeling plots in terrestrial carbon cycle research. *Glob. Biogeochem. Cycles* **2003**, *17*, 1022. [CrossRef]
47. Fischer, H.; Wahlen, M.; Smith, J. Reconstruction of glacial/interglacial changes in the global carbon cycle from CO_2 and $d^{13}CO_2$ in Antarctic ice cores. *Mem. Natl. Inst. Polar Res. Spec. Issue* **2003**, *57*, 121–138.
48. Köhler, P.; Fischer, H.; Schmitt, J.; Munhoven, G. On the application and interpretation of Keeling plots in paleo climate research—Deciphering $d^{13}CO_2$ of atmospheric CO_2 measured in ice cores. *Biogeosciences* **2006**, *3*, 539–556. [CrossRef]
49. Etiope, G.; Vadillo, I.; Whiticar, M.J.; Marques, J.M.; Carreira, P.M.; Tiago, I.; Benavente, J.; Jiménez, P.; Urresti, B. Abiotic methane seepage in the Ronda peridotite massif, southern Spain. *Appl. Geochem.* **2016**, *66*, 101–113. [CrossRef]
50. Whiticar, M.J. Carbon and hydrogen isotope systematics of bacterial formation and oxidation of methane. *Chem. Geol.* **1999**, *161*, 291–314. [CrossRef]
51. Thielemann, T.; Lucke, A.; Schleser, G.H.; Littke, R. Methane exchange between coalbearing basins and the atmosphere: The Ruhr Basin and the Lower Rhine Embayment, Germany. *Org. Geochem.* **2000**, *31*, 1387–1408. [CrossRef]
52. Alsaab, D.; Elie, M.; Izart, A.; Sachsenhofer, R.F.; Privalov, V.A.; Suarez-Ruiz, I.; Martinez, L.; Panova, E.A. Distribution of thermogenic methane in Carboniferous coal seams of the Donets Basin (Ukraine): "Applications to exploitation of methane and forecast of mining hazards". *Int. J. Coal Geol.* **2009**, *78*, 27–37. [CrossRef]
53. EnergieAgentur NRW. *Mine Gas. An Energy Source in Northrhine-Westphalia*; EnergieAgentur NRW: Düsseldorf, Deutschland, 2009.
54. Milkov, A.V. Worldwide distribution and significance of secondary microbial methane formed during petroleum biodegradation in conventional reservoirs. *Org. Geochem.* **2011**, *42*, 184–207. [CrossRef]
55. Mills, C.T.; Amano, Y.; Slater, G.F.; Dias, R.F.; Iwatsuki, T.; Mandernack, K.W. Microbial carbon cycling in oligotrophic regional aquifers near the Tono Uranium Mine, Japan as inferred from $d^{13}C$ and $D^{14}C$ values of in situ phospholipid fatty acids and carbon sources. *Geochim. Cosmochim. Acta* **2010**, *74*, 3785–3805. [CrossRef]
56. Stępniewska, Z.; Kuźniar, A. Endophytic microorganisms—Promising applications in bioremediation of greenhouse gases. *Appl. Microbiol. Biotechnol.* **2013**, *97*, 9589–9596. [CrossRef] [PubMed]
57. Stępniewska, Z.; Goraj, W.; Kuźniar, A. Transformation of methane in peatland environments. *Leśne Prace Badawcze* **2014**, *75*, 101–110. [CrossRef]
58. Thomas, L. *Coal Geology*; John Wiley & Sons Ltd.: Chichester, UK, 2002.
59. Hunt, J.M.; Philp, R.P.; Kvenvolden, K.A. Early developments in petroleum geochemistry. *Org. Chem.* **2002**, *33*, 1025–1052. [CrossRef]

60. Horita, J.; Berndt, M.E. Abiogenic methane formation and isotopic fractionation under hydrothermal conditions. *Science* **1999**, *285*, 1055–1057. [CrossRef]
61. Etiope, G.; Ionescu, A. Low-temperature catalytic CO_2 hydrogenation with geological quantities of ruthenium: A possible abiotic CH_4 source in chromititerich serpentinized rocks. *Geofluids* **2015**, *15*, 438–452. [CrossRef]
62. Etiope, G.; Judas, J.; Whiticar, M.J. Occurrence of abiotic methane in the eastern United Arab Emirates ophiolite aquifer. *Arab. J. Geosci.* **2015**, *8*, 11345–11348. [CrossRef]
63. Ritter, J.R.R. The Seismic Signature of the Eifel Plume. In *Mantle Plumes—A Multidisciplinary Approach*; Ritter, J.R.R., Christensen, U.R., Eds.; Springer: Berlin/Heidelberg, Germany, 2007.
64. Jackson, R.B.; Down, A.; Phillips, N.G.; Ackley, R.C.; Cook, C.W.; Plata, D.L.; Zhao, K. Natural gas pipeline leaks across Washington, DC. *Environ. Sci. Technol.* **2014**, *48*, 2051–2058. [CrossRef] [PubMed]
65. Zazzeri, G.; Lowry, D.; Fisher, R.E.; France, J.L.; Butler, D.; Lanoisellé, M.; Nisbet, E.G. Identification of urban gas leaks and evaluation of methane emission inventories using mobile measurements. *Geophys. Res. Abstr.* **2017**, *19*, 14409.
66. Toutain, J.P.; Baubron, J.C. Gas geochemistry and seismotectonics: A review. *Tectonophysics* **1999**, *304*, 1–27. [CrossRef]